Editors' Suggestion

Elastic rate coefficients for Li+H_2 collisions in the calibration of a cold-atom vacuum standard

Constantinos Makrides
Joint Quantum Institute, College Park, Maryland 20742, USA
and Department of Physics, University of Maryland, College Park, Maryland 20742, USA

Daniel S. Barker, James A. Fedchak, Julia Scherschligt, and Stephen Eckel
National Institute of Standards and Technology, Gaithersburg, Maryland 20899, USA

Eite Tiesinga
Joint Quantum Institute, College Park, Maryland 20742, USA;
Joint Center for Quantum Information and Computer Science, College Park, Maryland 20742, USA;
and National Institute of Standards and Technology, Gaithersburg, Maryland 20899, USA

(Received 11 February 2019; published 29 April 2019)

Ongoing efforts at the National Institute of Standards and Technology in creating a cold-atom vacuum standard device have prompted theoretical investigations of atom-molecule collision processes that characterize its operation. Such a device will operate as a primary standard for the ultrahigh-vacuum and extreme-high-vacuum regimes. This device operates by relating loss of ultracold lithium atoms from a conservative trap by collisions with ambient atoms and molecules to the background density and thus pressure through the ideal gas law. The predominant background constituent in these environments is molecular hydrogen H_2. We compute the relevant Li+H_2 Born-Oppenheimer potential energy surface, paying special attention to its uncertainty. Coupled-channel calculations are then used to obtain total rate coefficients, which include momentum-changing elastic and inelastic processes. We find that inelastic rotational quenching of H_2 is negligible near room temperature. For a ($T = 300$)-K gas of H_2 and 1.0-μK gas of Li atoms prepared in a single hyperfine state, the total rate coefficients are $6.0(1) \times 10^{-9}$ cm^3/s for both ^{6}Li and ^{7}Li isotopes, where the number in parentheses corresponds to a one-standard-deviation combined statistical and systematic uncertainty. We find that a 10-K increase in the H_2 temperature leads to a 1.9% increase in the rate coefficients for both isotopes. For Li temperatures up to 100 μK, changes are negligible. Finally, a semiclassical Born approximation significantly overestimates the rate coefficients. The difference is at least ten times the uncertainty of the coupled-channel result.

DOI: 10.1103/PhysRevA.99.042704

I. INTRODUCTION

Efforts are ongoing to utilize laser-cooled atoms to improve metrological quantities, the most famous of which is the realization of SI time [1]. The strength of cold-atom realizations for metrological purposes comes from the fact that atoms can be meticulously controlled and manipulated. Here the focus is on the implementation of a cold-atom vacuum standard (CAVS) device that utilizes trapped cold atoms with temperatures on the order of 10 μK to accurately measure pressures in the ultrahigh-vacuum (UHV) ($p < 10^{-6}$ Pa) and extreme-high-vacuum (XHV) ($p < 10^{-10}$ Pa) regimes, where there is a lack of primary vacuometer [2,3]. The remaining background gases are typically near room temperature.

A common device in UHV and XHV vacuum metrology is the Bayard-Alpert ionization gauge [4]. This device operates by ionizing the molecules within a helical grid and measuring the resulting current on a nearby collector wire. Ionization gauges are calibrated at a known pressure. In contrast, in a CAVS charge-neutral cold sensor, atoms held in a shallow trap are ejected by collisions with background atoms and molecules with near unit likelihood. The number of trapped atoms exponentially decreases in time and the corresponding rate is directly related to background pressure, without the need for calibration.

The CAVS device is a natural outgrowth of cold-atom experiments that sought to prepare quantum degenerate gases, such as Bose-Einstein condensates [5–7], with long trap lifetimes. Early on, it was observed that a limiting factor to cold-atom lifetimes is losses from collisions with background atoms and molecules [8–11]. As these experiments are performed under UHV and XHV conditions, it is then natural to investigate the possibility to measure ambient pressure from losses [10,12–17]. In ideal conditions, the relationship between pressure and loss rates is only limited by the accuracy of collisional cross sections and collisional rate coefficients between the cold atoms and the background constituents. Background collisions are also expected to limit the accuracy of ultracold optical atomic clocks [18]. More recently, chains of atomic ions in a linear Paul trap have also been used to measure pressure [19].

To clarify, we outline the connection between the loss rate and pressure. First, the time evolution of the number of sensor atoms N_S satisfies [10]

$$dN_S/dt = -\Gamma N_S + O\left(N_S^2\right), \tag{1}$$

where the loss rate

$$\Gamma = K^{\mathrm{CAVS}}(T_{\mathrm{S}}, T_{\mathrm{BG}}) n_{\mathrm{BG}}, \tag{2}$$

with thermalized rate constant $K^{\mathrm{CAVS}}(T_{\mathrm{S}}, T_{\mathrm{BG}})$ and sensor and background temperatures T_{S} and T_{BG}, respectively. Finally, n_{BG} is the background gas density, where we have implicitly assumed that the background contains only a single constituent.

Formally, contributions to K^{CAVS} include only collisions that impart enough kinetic energy to eject the cold atom from its trap. These processes can be elastic momentum-changing, inelastic state-changing, or even reactive collisions. The effect of glancing-elastic collisions, which do not eject the atoms from their trap and simply heat the gas, can be mitigated by ensuring that the trap depth is sufficiently small [3,10]. Equation (1) additionally indicates the presence of higher-order effects $O(N_{\mathrm{S}}^2)$. These include inelastic collisions among the cold sensor atoms that eject one or more of the atoms from the trap. This effect is mitigated by preparing the cold atom in a single hyperfine state.

Through the ideal gas law the background pressure is

$$p_{\mathrm{BG}} = n_{\mathrm{BG}} k_{\mathrm{B}} T_{\mathrm{BG}} = \frac{\Gamma}{K^{\mathrm{CAVS}}} k_{\mathrm{B}} T_{\mathrm{BG}}, \tag{3}$$

where k_{B} is the Boltzmann constant. The background pressure is thus determined though a measurement of Γ and an independent determination of K^{CAVS}. The background temperature is typically well characterized in these experiments. The CAVS is a primary standard for pressure as it relies on immutable collisional properties of atoms and molecules. In other words, the device does not need calibration as opposed to ion gauges, which need to be periodically recertified.

Details of ongoing efforts at the National Institute of Standards and Technology (NIST) in developing a CAVS device including the efforts into miniaturization can be found in Refs. [2,3]. The NIST device will use either ^{6}Li or ^{7}Li as the cold sensor atom. In UHV and XHV systems, the most abundant molecule remaining is molecular hydrogen H_2. As such, we specialize this work to the nonreactive Li+H_2 collision and present near-first-principles calculations of $K^{\mathrm{CAVS}}(T_{\mathrm{Li}}, T_{\mathrm{H_2}})$ and its uncertainty using quantum-mechanical descriptions for both electronic potential surfaces and nuclear motion.

The LiH_2 system has been investigated previously in the context of chemical reactivity in the early universe [20,21]. In contrast to our work, these astrophysically important investigations focused on the reactive collision LiH + H → Li + H_2, which is an exothermic reaction releasing approximately $k_{\mathrm{B}} \times (2 \times 10^4\ \mathrm{K})$ worth of energy [21]. We have asked for and obtained Born-Oppenheimer potential energy surfaces (PESs) from Refs. [22,23], which were created by different computational approaches for the electronic motion. As their focus was on the reactive process, which is insensitive to the fine details of the PES near the Li+H_2 asymptote, and they do not provide estimates of the uncertainty in their potentials, we have opted to recompute the PES near the Li+H_2 asymptote.

This paper is organized as follows. A description of the coupled-channel equations that describe the nuclear motion is presented in Sec. II. The derivation closely follows the nonreactive collisions described in Refs. [24,25]. We highlight the peculiarities of our system. In Sec. III we describe the calculation of the Born-Oppenheimer PES. We then present intermediate results, some physical insights, and discuss the effect of small changes in the potentials in Sec. IV. Our final values for K^{CAVS} and its uncertainty are presented in Sec. V. We conclude in Sec. VI with a few remarks about systematic effects in the computation of K^{CAVS}.

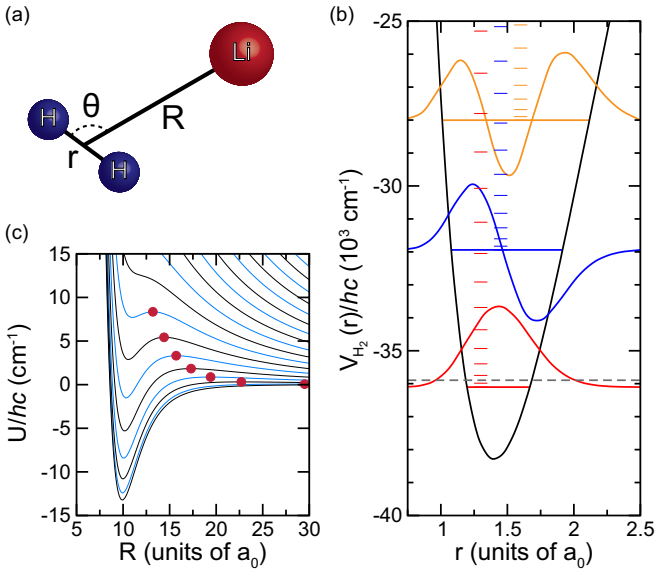

FIG. 1. (a) Jacobi coordinates r, R, and θ for Li+H_2 collisions. (b) Bottom part of the $X\,^1\Sigma_g^+$ potential of H_2 as a function of r. The zero of energy is at its dissociation limit. Energies of rovibrational states for $v = 0$, 1, and 2 are depicted by the red, blue, and orange horizontal lines within the potential, respectively. Energies of $j > 0$ rotational states are shown as shorter horizontal lines. The horizontal black dashed line is the total energy of a typical room-temperature collision of a $(v = 0, j = 0)$ H_2 molecule with lithium. Finally, the $v = 0, 1, 2$ and $j = 0$ radial wave functions $r\phi_{vj}(r)$ are also shown. (c) Isotropic atom-diatom potentials including the centrifugal potential $\hbar^2\ell(\ell+1)/2\mu R^2$ dissociating to the $v = j = 0$ state of H_2 as a function of R. Red markers indicate the location and energy of the top of the barriers. Curves for $\ell > 7$ are completely repulsive and have no minimum.

II. SCATTERING HAMILTONIAN

The Hamiltonian for the relative motion of nonreactive scattering of a lithium atom by a hydrogen molecule is

$$H = -\frac{\hbar^2}{2\mu}\nabla_R^2 - \frac{\hbar^2}{2\mu_{\mathrm{H_2}}}\nabla_r^2 + V(R, r, \theta) + H_{\mathrm{hf}}, \tag{4}$$

in the Jacobi coordinates $\vec{R}$ and $\vec{r}$ shown in Fig. 1(a). Here $\vec{R}$ is the vector from the center of mass of the hydrogen molecule to the lithium atom, $\vec{r}$ is the vector connecting the two hydrogen atoms, and θ is the angle between the vectors $\vec{R}$ and $\vec{r}$. The vector differential operator $\vec{\nabla}_x$ is with respect to $\vec{x}$. Moreover, μ is the reduced mass of the ^{6,7}Li + H_2 system, $\mu_{\mathrm{H_2}}$ is the reduced mass of H_2, and $\hbar = h/2\pi$, where h is Planck's constant. The operator $V(R, r, \theta)$ corresponds to the energetically lowest, doublet Born-Oppenheimer PES, which is a function of only the separations R and r and angle θ. When

all interatomic separations are large, $V(R, r, \theta)$ goes to zero. Its evaluation is discussed in the following section. Finally, the Hamiltonian $H_{\rm hf}$ contains the hyperfine interactions of the ground-state ^2S hydrogen and ^2S lithium atoms. In a CAVS device a small magnetic field is applied to be able to prepare Li in a specific hyperfine state. The corresponding Zeeman shifts from this magnetic field are negligible compared to the hyperfine interaction and are ignored in our scattering Hamiltonian.

The natural basis in which to perform scattering calculations for room-temperature Li+H_2 collisions is

$$|\mathrm{H_2}\rangle|\mathrm{Li}\rangle Y_{\ell m_\ell}(\hat{R}), \tag{5}$$

where the $Y_{\ell m_\ell}(\hat{R})$ are spherical harmonics that describe the rotation of Li and H_2 about each other with orbital angular momentum quantum number ℓ and space-fixed projection m_ℓ, and $\hat{R}$ is the orientation of $\vec{R}$ in our coordinate system. The kets $|\mathrm{Li}\rangle$ and $|\mathrm{H_2}\rangle$ represent atomic basis functions for Li and H_2, respectively. The lithium atom is trapped in a single hyperfine state $|\mathrm{Li}\rangle = |(S_{\rm Li}, I_{\rm Li})F_{\rm Li}m_{\rm Li}\rangle$, where the total atomic angular momentum $\vec{F}_{\rm Li} = \vec{S}_{\rm Li} + \vec{I}_{\rm Li}$, $S_{\rm Li} = 1/2$, and $I_{\rm Li} = 1$ and $3/2$ for ^{6}Li and ^{7}Li, respectively. Projection quantum numbers are with respect to a space-fixed coordinate system. We follow Ref. [26] for angular momentum algebra.

The kets

$$|\mathrm{H_2}\rangle \equiv \phi_{vj}(r)Y_{jm_j}(\hat{r})|Sm_S\rangle|Im_I\rangle \tag{6}$$

represent the rovibrational levels of the $X\,^1\Sigma_g{}^+$ state of H_2, where $\phi_{vj}(r)$ are unit-normalized vibrational wave functions with vibrational quantum number v and orbital angular momentum quantum j, and $Y_{jm_j}(\hat{r})$ are spherical harmonics that describe its rotation. The ket $|Sm_S\rangle$ represents the electronic wave function of the $X\,^1\Sigma_g{}^+$ state with total electronic angular momentum quantum number $S = 0$ and projection $m_S = 0$, while $|Im_I\rangle$ describes the nuclear spin wave function of the two protons. Orthohydrogen and parahydrogen correspond to states with $I = 0$ and 1, respectively. Moreover, identical particle statistics enforces that even rotational states j have $I = 0$, while odd j have $I = 1$. Consequently, H_2 wave functions are uniquely specified by $|\mathrm{H_2}\rangle = |v, jm_j\rangle$ with energy ϵ_{vj} independent of m_j and nuclear spin quantum numbers as we can neglect the hyperfine interactions of a singlet molecule in $H_{\rm hf}$. The lowest rovibrational energy levels are shown in Fig. 1(b). It follows that only the lowest few rotational levels of the $v = 0$ state are populated in a room-temperature gas.

The implicit approximations in the discussion thus far are justified in Appendix A. The approximations allow us to define the coupled basis

$$|v; (j, \ell)JM\rangle \equiv \phi_{vj}(r)|(j, \ell)JM\rangle \times |Sm_S = 00\rangle|(S_{\rm Li}, I_{\rm Li})F_{\rm Li}m_{\rm Li}\rangle, \tag{7}$$

with

$$|(j, \ell)JM\rangle = \sum_{m_j m_\ell} \langle JM|j\ell, m_j m_\ell\rangle Y_{jm_j}(\hat{r})Y_{\ell m_\ell}(\hat{R}), \tag{8}$$

where $\langle JM|j\ell, m_j m_\ell\rangle$ is a Clebsch-Gordan coefficient. In the ket $|v; (j, \ell)JM\rangle$, the labels for the hyperfine states are suppressed as they are conserved independently. Our Hamiltonian H commutes with J_z and the parity operation and thus only states with the same $p = (-1)^{j+\ell}$ are coupled. Finally, we write the Hamiltonian as

$$H = -\frac{\hbar^2}{2\mu}\nabla_R^2 + H_{\mathrm{H_2}} + U(R, r, \theta), \tag{9}$$

where $H_{\mathrm{H_2}} \equiv -\hbar^2\nabla_r^2/2\mu_{\mathrm{H_2}} + V_{\mathrm{H_2}}(r)$ is the Hamiltonian of the hydrogen molecule, $V_{\mathrm{H_2}}(r)$ is the $X\,^1\Sigma_g{}^+$ potential, and $U(R, r, \theta) \equiv V(R, r, \theta) - V_{\mathrm{H_2}}(r)$. In this form, $H_{\mathrm{H_2}}$ is diagonal in our basis $|v; (j, \ell)JM\rangle$.

Scattering states of H are found by using a coupled-channel approach, which leads to a set of coupled ordinary second-order differential equations with respect to R, one for each basis-set element. We then require matrix elements of $U(R, r, \theta)$, which will be described in the next section. The numerical procedure to solve the coupled-channel equations follows the method of Johnson [27]. Specifically, the logarithmic derivative of the wave function is propagated to sufficiently large R with a variable step size that changes according to variations in the amplitudes of the solutions. The dimensionless unitary S matrix is formally extracted from the solutions at $R \to \infty$ [28], however, we find it sufficient to extract S-matrix elements from the solutions at $R = 5000a_0$. In particular, for each J, M, and energy $E > \epsilon_{v=0,j=0}$, we obtain the S-matrix elements $s^{(J)}_{\alpha',\alpha}(E)$ for the transition from $\alpha = \{v, j, \ell\}$ to $\alpha' = \{v', j', \ell'\}$. The matrix elements are independent of M.

The rate coefficient $K^{\rm CAVS}(T_{\rm Li}, T_{\mathrm{H_2}})$ includes all collision processes that remove a sensor atom from the trap. For the ideal CAVS, where the glancing collisions have a negligible influence, this corresponds to the computation of the total cross section or total rate coefficient. We will also show results for the energy-dependent state-to-state rate coefficients $K_{v'j',vj}(E)$ and the corresponding thermally averaged rate coefficients $L_{v'j',vj}(T_{\rm Li}, T_{\mathrm{H_2}})$. The exact definition of these quantities and their connection to $K^{\rm CAVS}(T_{\rm Li}, T_{\mathrm{H_2}})$ are given in Appendix B. Specifically, we show that $K^{\rm CAVS}$ is only a function of

$$T_{\rm eff} = \frac{m_{\mathrm{H_2}}}{m_{\rm Li} + m_{\mathrm{H_2}}}T_{\rm Li} + \frac{m_{\rm Li}}{m_{\rm Li} + m_{\mathrm{H_2}}}T_{\mathrm{H_2}}. \tag{10}$$

III. POTENTIAL ENERGY SURFACE

The rate coefficient $K^{\rm CAVS}(T_{\rm Li}, T_{\mathrm{H_2}})$ depends on the potentials $V(R, r, \theta)$ and $V_{\mathrm{H_2}}(r)$. The trimer potential is the $^2A'$ ground-state surface, which approaches the $X\,^1\Sigma_g{}^+$ potential of H_2 when the lithium atom is far away. We have used the complete active space self-consistent field (CASSCF) and multireference configuration-interaction (MRCI) programs within the MOLPRO suite [29] to calculate the two potentials. The inner 1s electrons of Li form our frozen core. Correlations in the MRCI program only include those among the three other electrons in LiH_2.

The augmented, correlation-consistent, polarized valence basis sets [30,31] are used for hydrogen and weighted core variants for lithium [32]. The bases are aug-cc-pVxZ and aug-cc-pwCVxZ with x = T, Q, and 5 for hydrogen and lithium, respectively. The sequence corresponds to a progression of larger basis sets, leading to ever more accurate PESs, labeled $V^{xZ}(R, r, \theta)$. We correct for the basis-set superposition error with the counterpoise (CP) correction algorithm of Ref. [33].

Next we extrapolate the PESs to the complete-basis-set (CBS) limit $V^{\infty Z}(R, r, \theta)$. It is found by solving the linear system of three equations [34,35]

$$V^{xZ} = V^{\infty Z} + Be^{-(x-1)} + Ce^{-(x-1)^2} \tag{11}$$

at every R, r, and θ, where $V^{\infty Z}$, B, and C are the unknowns. In Eq. (11) we use $x = 3$, 4, and 5 for basis sets T, Q, and 5, respectively. We have also computed the $X\,^1\Sigma_g^+$ potential of H_2 with these bases.

The choice of methods, frozen electrons, and other corrections (i.e., counterpoise and Davidson corrections as well as the CBS extrapolation) is a compromise between computing the PES sufficiently accurate and the computational cost. In Appendix C we elucidate our choices and provide an assessment of the uncertainty in $V^{\infty Z}(R, r, \theta)$. More details about this uncertainty and its effect on rate coefficients are found in Sec. V.

Within the coupled-channel approach, it is convenient to express the PES in terms of Legendre polynomials in $\cos\theta$. That is, we define

$$U(R, r, \theta) = \sum_{\lambda=0}^{\infty} \left[V_\lambda(R, r) - \delta_{\lambda,0} V_{H_2}(r)\right] P_\lambda(\cos\theta), \tag{12}$$

where $V_\lambda(R, r)$ are radial strength functions, $P_\lambda(\cos\theta)$ are Legendre polynomials, and $\delta_{i,j}$ is the Kronecker delta function. We omit superscripts xZ from the potentials to keep the expressions simple. The matrix elements of the potential $U(R, r, \theta)$ in our basis $|v; (j, \ell)JM\rangle$ are

$$\langle v'; (j', \ell')JM|U(R, r, \theta)|v; (j, \ell)JM\rangle = \sum_{\lambda=0}^{\infty} \langle (j', \ell')JM|P_\lambda(\cos\theta)|(j, \ell)JM\rangle\, \Xi^\lambda_{v'j',vj}(R), \tag{13}$$

where $\langle (j', \ell')JM|P_\lambda(\cos\theta)|(j, \ell)JM\rangle$ are the Percival-Seaton coefficients [36], which are only nonzero when both $\ell + \lambda + \ell'$ and $j + \lambda + j'$ are even. In addition, various triangular conditions hold between the angular momenta; in particular, it holds for j, λ, and j'. The rovibrationally averaged matrix elements

$$\Xi^\lambda_{v'j',vj}(R) = \int_0^\infty r^2 dr\, \phi^*_{v'j'}(r) \left[V_\lambda(R, r) - \delta_{\lambda,0} V_{H_2}(r)\right] \phi_{vj}(r) \tag{14}$$

are functions of R.

Figure 2 shows strength functions $V_\lambda^{xZ}(R, r_0)$ for the family of potentials and $\lambda = 0$, 2, and 4 as functions of R with $r_0 = 1.4a_0$, near the equilibrium separation of H_2. For the homonuclear H_2 only the even λ strength functions are nonzero. The isotropic $\lambda = 0$ strength function has a depth of at most $V_0/hc = 12$ cm^{-1} at $R \approx 10a_0$, where c is the speed of light in vacuum. This isotropic potential conserves partial wave ℓ, while potential functions with $\lambda > 0$ are anisotropic and can couple different partial waves as long as $|\ell' - \ell| \leqslant \lambda$. The $\lambda = 2$ strength function is the largest anisotropic potential and will lead to most of our couplings. The depth and sizes of the $V_\lambda^{xZ}(R, r)$ are not unique to our system. Reference [25] shows similar strength functions as a function of R for Na+N_2.

Both the rotational spacings of H_2 and the room-temperature collision energies are at least an order of magnitude larger than any of the strength functions within the classically accessible domain. Consequently, the effects of coupling by the $\lambda > 0$ radial strength functions are expected to be small and that the scattering is driven by the isotropic potential.

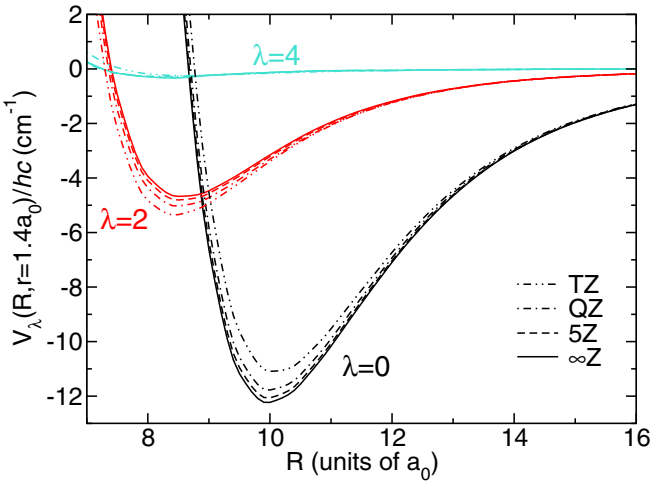

FIG. 2. Radial strength functions $V_\lambda^{xZ}(R, r_0)$ as a function of R with $r_0 = 1.4a_0$, near the equilibrium separation of H_2. For each λ, the solid, dashed, dot-dashed, and double-dot–dashed lines represent the strength functions for $x =$ T, Q, 5, and ∞, respectively. For $\lambda = 0$, we plot $V_0^{xZ}(R, r) - V_0^{xZ}(R \to \infty, r_0)$. For $\lambda > 0$, $V_\lambda^{xZ}(R, r_0)$ goes to zero when $R \to \infty$.

Figure 2 also shows that the depth of the isotropic $\lambda = 0$ strength function increases as the basis-set size increases. Specifically, the depth of $V_{\lambda=0}^{xZ}(R, r_0)/hc$ is 11.1, 11.7, 12.1, and 12.2 cm^{-1} for $x =$ T, Q, 5, and ∞, respectively. In contrast, the anisotropic $\lambda = 2$ strength function becomes progressively weaker. These observations will be used in Sec. IV, where the uncertainty of K^{CAVS} is characterized.

For sufficiently large separations R, the potential $U(R, r, \theta)$ of Eq. (12) connects to the long-range dispersion potential

$$-\frac{1}{R^6}[C_{6,0}(r) + C_{6,2}(r)P_2(\cos\theta)], \tag{15}$$

where $C_{6,0}(r)$ and $C_{6,2}(r)$ are the isotropic and anisotropic dispersion coefficients between H_2 and Li, respectively [37]. Equivalently, $V_\lambda(R, r) \to -C_{6,\lambda}(r)/R^6$ for $\lambda = 0$ and 2. For $\lambda > 2$, the long-range potential falls off as $1/R^8$ or faster.

Figures 3(a) and 3(b) show $C_{6,0}(r)$ and $C_{6,2}(r)$ as functions of r, respectively. The isotropic $C_{6,0}(r)$ increases by a factor of 3 within the range shown. For $r > 3.0a_0$, not shown here, $C_{6,0}(r)$ turns over and approaches from above twice the value of the Li-H dispersion coefficient. The markers in Fig. 3 are from Ref. [39]. The isotropic values have a 0.1% one standard uncertainty. The solid lines are interpolated and extrapolated from the markers and are used in our scattering calculation. The anisotropic $C_{6,2}(r)$ also increases with r, but is at most 1/5 as large as $C_{6,0}(r)$, as is shown in Fig. 3(c).

Appendix D contains details about the grid on which the *ab initio* potentials are computed. The chosen grid minimizes the need to interpolate, thus minimizing fitting errors. We show how to construct $C_{6,0}(r)$ and $C_{6,2}(r)$ from the values in Ref. [39] and how to continuously connect the short-range

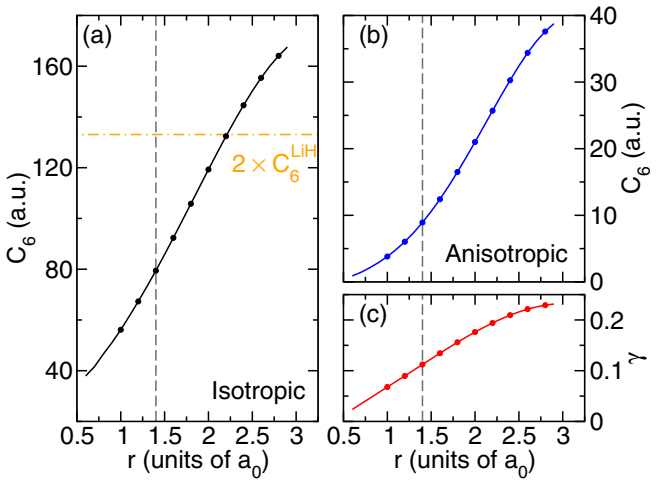

FIG. 3. Dispersion coefficients of the Li-H_2 system. (a) Isotropic dispersion coefficient $C_{6,0}$ as a function of H-H separation r. The horizontal dot-dashed line corresponds to twice the value of the dispersion coefficient of Li and H atoms [38]. Also shown are (b) the anisotropic dispersion coefficient $C_{6,2}$ and (c) $\gamma \equiv C_{6,2}/C_{6,0}$ as a function of r. The vertical dashed line in all panels corresponds to the equilibrium separation of H_2. The markers in all panels are from Ref. [39] and the curves are our interpolated and extrapolated values. The uncertainty in the markers in (a) is negligible on the scale of the graph.

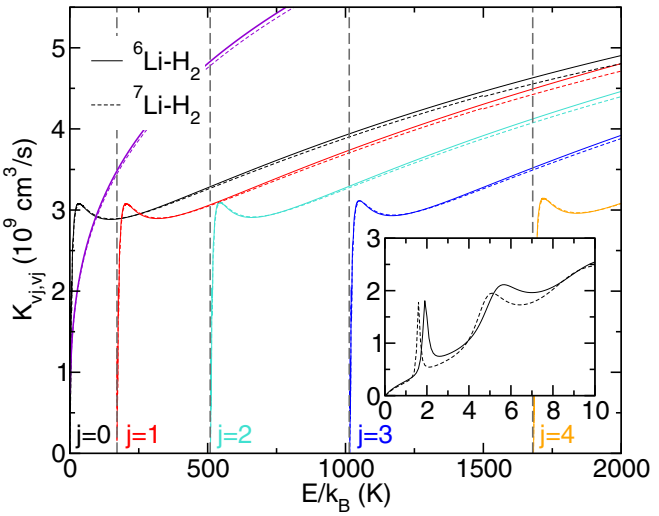

FIG. 4. Elastic rate coefficients $K_{vj,vj}(E)$ for $^{6,7}\mathrm{Li} + \mathrm{H}_2(v = 0, j)$ as functions of energy with respect to $\epsilon_{v=0,j=0}$ based on the ∞Z potential surface. The black, red, turquoise, blue, and orange lines correspond to coefficients with $j = 0$, 1, 2, 3, and 4, respectively. Solid and dashed lines are for the ^{6}Li and ^{7}Li isotopes, respectively. Vertical lines indicate energies where rotational states j become energetically accessible. Purple lines are Born approximations for the elastic rate of the $j = 0$ state. The inset shows $K_{00,00}(E)$ for the low-energy region where shape resonances are pronounced. The shape resonances near $E/k_B = 2$ and 6 K are due to g-wave ($\ell = 4$) and h-wave ($\ell = 5$) collisions, respectively. The resonances are shifted to smaller energies for the heavier isotope. (Data up to 3000 K are available, but not shown.)

ab initio potentials to the long-range ones by adding a small corrective $1/R^8$ potential. For our purposes, we do not require the dispersion coefficients for $r > 2.5a_0$. Finally, we describe the evaluation of H_2 wave functions $\phi_{vj}(r)$ and energies ϵ_{vj}.

We supply the necessary data files to compute the matrix elements $\Xi^{\lambda}_{v',j',c,j}(R)$ in the Supplemental Material [40]. Specifically, the CBS extrapolated radial strength functions $V_\lambda(R, r)$ are provided for $\lambda = 0$, 2, and 4; $r \in (r_{\min}, r_{\max})$; and $R \in (3.5a_0, 20.0a_0)$. Here $r_{\min} = 0.5a_0$ and $r_{\max} = 2.5a_0$. We also supply the interpolated and extrapolated values for $C_{6,\lambda}(r)$ for $\lambda = 0$ and 2 with $r \in (r_{\min}, r_{\max})$. Finally, we include the $X\,^1\Sigma_g^+$ H_2 potential for $r \in (r_{\min}, r_{\max})$.

IV. RESULTS

We have computed S-matrix elements $s^{(J)}_{\alpha',\alpha}(E)$ for energies E above $\epsilon_{v=0,j=0}$ up to $k_B \times 3000$ K and angular momenta J up to 125 or 200 (for $E < k_B \times 2000$ K we use $J \leqslant 125$ and 200 otherwise). For these energies, only the first six rotational states of the $v = 0$ vibrational state of H_2 can be accessed. The step size in the energy grid alternates between $k_B \times 0.1$ and $k_B \times 1$ K. It is 0.1 K when $E/k_B \in (\epsilon_{v,j} - \epsilon_{0,0})/k_B + [0.1\text{ K}, 50\text{ K}]$ and $k_B \times 1$ K otherwise. This choice anticipates the presence of shape resonances in the scattering. Figure 1(c) shows the isotropic potential $\Xi^{\lambda=0}_{00,00}(R) + \hbar^2\ell(\ell+1)/2\mu R^2$ for the $(v = 0, j = 0)$ state of H_2. In fact, $\Xi^{\lambda=0}_{00,00}(R) = V_{\lambda=0}(R, r_e)$ to a good approximation. We see that any shape resonance must occur for $\ell \leqslant 7$ and $E < k_B \times 15$ K, justifying the finer energy grid above each threshold. The upper bounds on E and J ensure thermalized rate coefficients that are accurate to better than 0.5% for temperatures up to 350 K.

Figure 4 shows the energy-dependent elastic rate coefficient $K_{vj,vj}(E)$ for both ^{6}Li and ^{7}Li isotopes based on the $V^{\infty Z}(R, r, \theta)$ PES. The lithium atoms are prepared in a single hyperfine state. The difference in $K_{vj,vj}(E)$ for the two Li isotopes is at most 2.5% away from shape resonances. The figure also shows the rate coefficient based on the Born approximation for the isotropic long-range dispersion potential. This theory was developed in the 1960s and is often used in the description of room-temperature collisions [41,42]. It is given by

$$K_{\mathrm{BA}}(E) = \kappa \frac{\hbar\beta_6}{\mu}(E/E_6)^{3/10}, \tag{16}$$

where $\kappa = 6.125\,601\,46\ldots$, and $\beta_6 = (2\mu C_{6,0}/\hbar^2)^{1/4}$ and $E_6 = \hbar^2/2\mu\beta_6^2$ are length and energy scales for a $-C_{6,0}/R^6$ potential, respectively. Surprisingly, the disagreement between this prediction and the coupled-channel result is large, especially for room-temperature energies and above, where the approximation might be expected to be valid. This disparity cannot be accounted for by the uncertainty in the $C_{6,0}(r)$ coefficients. A detailed explanation for this disagreement can be found in Appendix E, where we compare scattering phase shifts.

The inset in Fig. 4 shows two shape resonances in the $j = 0$ elastic rate coefficient, occurring at energies below $k_B \times 10$ K. The two resonances have partial wave $\ell = 4$ and 5 character, respectively. A broader $\ell = 6$ resonance (not shown) around $k_B \times 12$ K also exists. We do not see evidence of shape

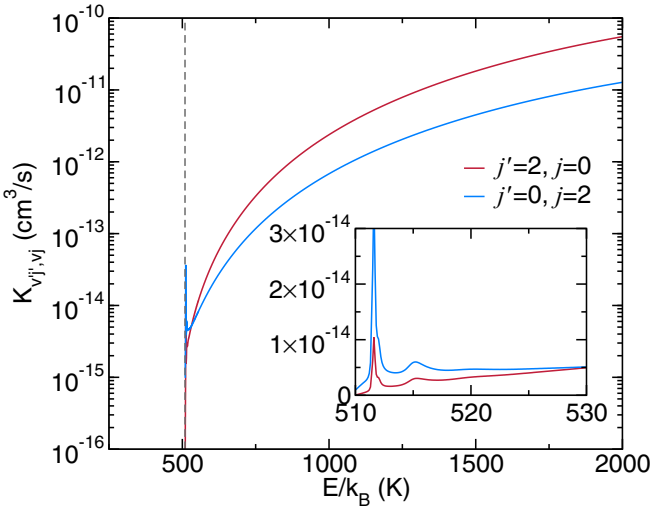

FIG. 5. Inelastic rate coefficients $K_{v'j',vj}(E)$ as functions of energy for $v' = v = 0$ based on the ∞Z potential surface. The blue and red curves correspond to transitions from $j = 2$ to $j' = 0$ and from $j = 0$ to $j' = 2$, respectively. The vertical dashed line is the channel opening energy at $\epsilon_{v=0,j=2}$. The inset magnifies the region between $E/k_B = 510$ and 530 K, where there are two shape resonances.

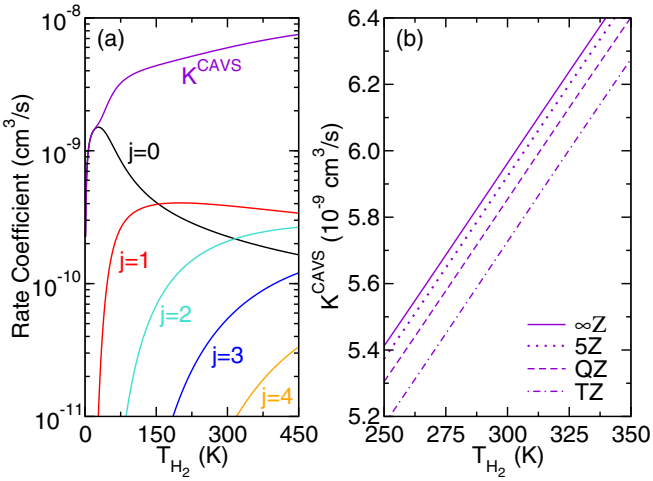

FIG. 6. (a) Thermalized rate coefficients $L_{vj,vj}(T_{Li}, T_{H_2})$ for $v = 0$, $j = 0, 1, 2, \ldots$, and $K^{CAVS}(T_{Li}, T_{H_2})$ as functions of the H_2 temperature with ^{6}Li cold sensor atoms at $T_{Li} = 1$ μK, using the ∞Z PES. The purple line is K^{CAVS}, while the black, red, turquoise, blue, and orange lines show $L_{vj,vj}$ for $j = 0$, 1, 2, 3, and 4, respectively. (b) Thermalized $K^{CAVS}(T_{Li}, T_{H_2})$ as a function of T_{H_2} around room temperature. The dot-dashed, dashed, dotted, and solid lines correspond to thermalized rate coefficients based on the TZ, QZ, 5Z, and ∞Z PESs.

resonances with widths narrower than $k_B \times 0.1$ K. Similar resonant features are found for ($v = 0$, $j > 0$) collisions.

The rate coefficients $K_{vj,vj}(E)$ for different j quickly rise from $E = \epsilon_{v,j}$ to $E = \epsilon_{v,j} + (k_B \times 30\ \text{K})$ and then show a gentle increase with energy. For all rotational states of H_2, the $K_{vj,vj}(E)$ are functionally similar save for a shift in energy.

The anisotropic strength functions are responsible for inelastic j-changing collisions. Parity conservation prevents even- and odd-j-state coupling, therefore the first energetically allowed inelastic process is between the $j = 0$ and 2 states. Figure 5 shows $K_{v'j',vj}(E)$ for these inelastic processes. The rate coefficient is zero below the channel opening threshold at $E = \epsilon_{v=0,j=2} - \epsilon_{v=0,j=0} \approx k_B \times 510$ K and then increases to a few times 10^{-11} cm^3/s, two orders of magnitude smaller than the corresponding elastic rate coefficient. Consequently, for room-temperature collisions, the effects of inelastic processes on the CAVS device are weak and indicate that anisotropic strength functions can be ignored. In fact, from calculations where only the $\lambda = 0$ strength function is included, we find that the elastic $K_{vj,vj}(E)$ changes by less than 1% away from the shape resonances. A small inelastic rate coefficient is not unprecedented. Loreau *et al.* [25] found similar values for the Na+N_2 collision, which has the same spin structure as Li+H_2.

Figure 6(a) shows the thermalized rate constants $L_{vj,vj}(T_{Li}, T_{H_2})$ for the ^{6}Li isotope as a function of T_{H_2} with $T_{Li} = 1$ μK, obtained from thermalizing $K_{vj,vj}(E)$. Also shown in Fig. 6(a) is $K^{CAVS}(T_{Li}, T_{H_2})$, which is a weighted sum of the $L_{vj,vj}(T_{Li}, T_{H_2})$. For H_2 temperatures below 100 K, K^{CAVS} is dominated by the contribution from the $j = 0$ rotational state, while at room temperatures $j = 0$, 1, and 2 states contribute significantly. The shape resonances do not significantly contribute to the thermalized rate coefficients near room temperature. Rate constants at other ^{6}Li temperatures can be obtained using T_{eff} defined in Appendix B.

Figure 6(b) shows K^{CAVS} for the four potentials constructed in the preceding section as a function of T_{H_2} in a 100-K region centered at 300 K. There is a progression to larger K^{CAVS} for larger basis sets, corresponding to deeper isotropic potentials. The difference in the rate coefficients computed for the four potentials is rather small with the 5Z to QZ difference equal to approximately 1% at $T_{H_2} = 300$ K.

Functionally, $K^{CAVS}(T_{Li}, T_{H_2})$ is close to linear for each potential and is well represented by a Taylor expansion to second order in T_{H_2} around $T_{ref} \equiv 300$ K and first order in T_{Li} around 1 μK. Noting that the rate coefficient only depends on T_{eff}, we have

$$K^{CAVS}(T_{Li}, T_{H_2}) = \mathcal{K}_0 + \mathcal{K}_1 (T_{H_2} - T_{ref}) + \frac{1}{2}\mathcal{K}_2 (T_{H_2} - T_{ref})^2 + \frac{m_{H_2}}{m_{Li}}\mathcal{K}_1 (T_{Li} - 1\ \mu\text{K}), \quad (17)$$

with expansion coefficients $\mathcal{K}_i$. This expansion reproduces the coupled-channel result to about 0.1% for a ±50-K region around $T_{H_2} = T_{ref}$ for each of the potentials. The dependence on the Li temperature up to 100 μK is negligible, but included for completeness.

V. PREDICTIONS FOR RATE COEFFICIENTS AND THEIR UNCERTAINTIES

Table I contains the final values and uncertainty for K^{CAVS} for both ^{6}Li-H_2 and ^{7}Li-H_2 through the expansion coefficients $\mathcal{K}_{0,1,2}$ defined in Eq. (17). The uncertainty in $K^{CAVS}(T_{Li}, T_{H_2})$ is fully determined by those in the interaction potential $V(R, r, \theta)$. The uncertainty from solving the coupled-channel

TABLE I. Values and one-standard-deviation uncertainties for $\mathcal{K}_0$, $\mathcal{K}_1$, and $\mathcal{K}_2$ of the thermalized total rate coefficient $K^{\mathrm{CAVS}}(T_{\mathrm{Li}}, T_{\mathrm{H_2}})$ as defined in Eq. (17) for near-room-temperature hydrogen molecules and 1-μK ^{6,7}Li sensor atoms with $T_{\mathrm{ref}} = 300$ K. The uncertainty $\sigma(K^{\mathrm{CAVS}})$ is found by error propagation with correlation coefficients $r(\mathcal{K}_i, \mathcal{K}_j) = 1$ when $i \neq j$.

Sensor atom	$\mathcal{K}_0$ ($\mathrm{cm^3/s}$)	$\mathcal{K}_1$ ($\mathrm{cm^3/s/K}$)	$\mathcal{K}_2$ ($\mathrm{cm^3/s/K^2}$)
^{6}Li	$6.0(1)\times10^{-9}$	$1.1062(9)\times10^{-11}$	$-1.1(2)\times10^{-15}$
^{7}Li	$6.0(1)\times10^{-9}$	$1.1053(6)\times10^{-11}$	$-1.8(3)\times10^{-15}$

equations is negligible. To be precise, the uncertainty of and covariances between the $\mathcal{K}_i$ follows from the potentials $V^{x\mathrm{Z}}(R, r, \theta)$ with $x = \mathrm{T}$, Q, 5, and ∞ shown in Fig. 2. In principle, the relationship between $V^{x\mathrm{Z}}(R, r, \theta)$ and the thermalized rate coefficient is complicated. Instead, we focus on the isotropic radial strength functions $V^{x\mathrm{Z}}_{\lambda=0}(R, r_0)$ with $r_0 = 1.4a_0$ near the equilibrium separation of the H_2 molecule. We define

$$V_{\lambda=0}(R, r_0; \xi) \equiv V^{5\mathrm{Z}}_{\lambda=0}(R, r_0) + \xi W(R), \tag{18}$$

where $W(R) \equiv |V^{\mathrm{QZ}}_{\lambda=0}(R, r_0) - V^{5\mathrm{Z}}_{\lambda=0}(R, r_0)|$ is the difference potential between our two best evaluations of the potential surface and ξ is an R-independent dimensionless scale factor that enables us to change the depth of the isotropic potential. The potential $V_{\lambda=0}(R, r_0; \xi)$ reproduces $V^{x\mathrm{Z}}_{\lambda=0}(R, r_0)$ for $x = \mathrm{T}$, Q, 5, and ∞ reasonably with $\xi = 3.5(5)$, 1.0, 0.0, and $-0.58(2)$, respectively. The uncertainty reflects the degree to which ξ is constant as a function of R. Empirically, we also find that $W(R, r_0) \approx W_0 \exp(-0.5R/a_0)$, which is negligible for $R > 15a_0$.

We characterize the uncertainties in the potentials by treating the factor ξ as a Gaussian-distributed random variable, where our best guess of the potential is at $\xi = \xi^{\infty\mathrm{Z}} = -0.58$ with a one-standard-deviation uncertainty $\sigma(\xi) = |\xi^{\mathrm{QZ}} - \xi^{\infty\mathrm{Z}}| = 1.58$. We are led to this conclusion because the increase in the isotropic potential depth with increasing basis-set size is incrementally becoming smaller. As such, the QZ basis serves as an upper bound on the true potential and the ∞Z potential as our best guess at the true potential. The 1-σ interval encapsulates the QZ, 5Z, and ∞Z potentials. The analysis found in Appendix C also suggests that other approaches in computing the PES lie within this uncertainty. We reach the same conclusions for different choices of r in Eq. (18).

For each of our potentials we have computed $\mathcal{K}_i(\xi)$ for $i = 0$, 1, and 2 and find that

$$\mathcal{K}_i(\xi) = \kappa_{i,0} + \kappa_{i,1}(\xi - \xi^{\infty\mathrm{Z}}) \tag{19}$$

near $\xi = \xi^{\infty\mathrm{Z}}$ with coefficients $\kappa_{i,j}$. The uncertainty in $K^{\mathrm{CAVS}}(T_{\mathrm{Li}}, T_{\mathrm{H_2}}; \xi)$ is then

$$\sigma^2(K^{\mathrm{CAVS}}) = \sum_{i,j} \frac{\partial K^{\mathrm{CAVS}}}{\partial \mathcal{K}_i} \frac{\partial K^{\mathrm{CAVS}}}{\partial \mathcal{K}_j} r(\mathcal{K}_i, \mathcal{K}_j)\sigma(\mathcal{K}_i)\sigma(\mathcal{K}_j) \tag{20}$$

with individual uncertainties

$$\sigma(\mathcal{K}_i) = \kappa_{i,1}\sigma(\xi) \tag{21}$$

and correlation coefficients $r(\mathcal{K}_i, \mathcal{K}_j)$. The distribution of the $\mathcal{K}_i$ are solely characterized by that of the random variable ξ, which implies that they are completely correlated and hence $r(\mathcal{K}_i, \mathcal{K}_j) = 1$. In other words, we equivalently write

$$\sigma(K^{\mathrm{CAVS}}) = \left[\kappa_{0,1} + \kappa_{1,1}\left(T_{\mathrm{H_2}} - T_{\mathrm{ref}}\right) + \tfrac{1}{2}\kappa_{2,1}\left(T_{\mathrm{H_2}} - T_{\mathrm{ref}}\right)^2\right]\sigma(\xi). \tag{22}$$

The $\kappa_{0,1}$ terms are the dominant contributors to $\sigma(K^{\mathrm{CAVS}})$ by at least three orders of magnitude.

VI. CONCLUSION

We have presented our findings on the collisional properties of the Li+H_2 system with applications to a CAVS device. We find that the elastic collisions dominate the thermally averaged rate coefficient $K^{\mathrm{CAVS}}(T_{\mathrm{Li}}, T_{\mathrm{H_2}})$ for a room temperature H_2 gas with a 1-μK temperature Li gas. Table I contains our final values and their uncertainties of $K^{\mathrm{CAVS}}(T_{\mathrm{Li}}, T_{\mathrm{H_2}})$ for both ^{6}Li and ^{7}Li isotopes. The uncertainty is less than 2% within a 100-K window centered around room-temperature H_2 molecules. The main source of the uncertainty is due to imprecisions in the computed potential energy surface and has been estimated by trends with increasing basis-set size. In principle, the evaluation of the PES with a larger basis set is expected to approach the true potential, at the cost of becoming numerically expensive. Feedback from experimental measurements can put further constraints on the potentials. This can be achieved with precise measurements of resonant features in rate coefficients that occur in collisions below $k_{\mathrm{B}} \times 10$ K. For example, the location of the shape resonance near $E \approx k_{\mathrm{B}} \times 2$ K shifts when the depth of the isotropic potential is changed, although the measurement would require approximately 100-mK sensitivity. The spectroscopic determination of trimer bound states can provide similar constraints.

We finish by describing systematic corrections that have been left out in our description, such as relativistic and nonadiabatic corrections. Relativistic effects are important for heavy systems and can be neglected here as LiH_2 is one of lightest trimers possible. Nonadiabatic effects arising from the coupling of different electronic states by the nuclear kinetic energy operator have been mitigated by using atomic masses rather than nuclear masses as would be dictated by the Born-Oppenheimer approximation. We conclude that nonadiabatic corrections are negligible because the fractional change in mass is orders of magnitude smaller than the corresponding change between ^{6}Li and ^{7}Li. The difference in $K^{\mathrm{CAVS}}(T_{\mathrm{Li}}, T_{\mathrm{H_2}})$ for ^{6}Li and ^{7}Li is less than 1% and is encompassed by the uncertainty in the PESs. Furthermore, conical intersections are inaccessible for our collision energies.

Finally, the true loss characteristics of ultracold Li in a CAVS also depend on collisions with constituents other than H_2 in the vacuum. These constituents include residual hot Li atoms that are a by-product of the trapping process, other ambient vacuum molecules, and any deliberately added gases to the vacuum. The first can be mitigated by careful design of the CAVS device, while the latter two will be accounted for by relative gas sensitivity coefficients [2]. Moreover, many of these nonreactive collisions are computationally tractable. The number of glancing collisions, which do not lead to sensor

atom loss, can be minimized by lowering the trap depth. The uncertainty in pressure (or equivalently background gas density) is found through error propagation based on Eq. (3) using the uncertainty in K^{CAVS} and the measurement uncertainty of the loss rate Γ. Thus, if the measurement uncertainty in Γ is larger than our uncertainty for K^{CAVS}, the resulting uncertainty in pressure will be limited by the experiment.

APPENDIX A: VALIDITY OF THE SCATTERING HAMILTONIAN

We have made several implicit approximations in our scattering Hamiltonian and basis set. In particular, we do not allow the molecule to break up into scattering states of the $X\,^1\Sigma_g{}^+$ potential or those of the $a\,^3\Sigma_u{}^+$ potential.[1] These approximation are justified as the $X\,^1\Sigma_g{}^+$ potential is 100 times deeper than the room-temperature collision energies. Furthermore, the reactive channel LiH+H is energetically inaccessible as it requires a collision energy of $E \approx k_{\mathrm{B}} \times 25\,000$ K with a $(v = 0, j = 0)$ hydrogen molecule.

There exist two doublet Born-Oppenheimer potentials that dissociate to the same limit for our triatomic system. When the lithium atom is well separated from the hydrogen atoms, the lowest trimer Born-Oppenheimer potential approaches that of the $X\,^1\Sigma_g{}^+$ state. The second trimer potential approaches that of the $a\,^3\Sigma_u{}^+$ state. This then justifies our usage of only the lower of the two trimer potentials. Equivalently, we have assumed that the electronic spin wave function of our trimer is $|(s_1, s_2)S, S_{\mathrm{Li}}; S_{\mathrm{tot}} m_{\mathrm{tot}}\rangle = |(1/2, 1/2)0, 1/2; 1/2, m_{\mathrm{tot}}\rangle$, where $\vec{s}_1$ and $\vec{s}_2$ are the electron spins of the individual hydrogen atoms, $\vec{S} = \vec{s}_1 + \vec{s}_2$, and $\vec{S}_{\mathrm{tot}} = \vec{S} + \vec{S}_{\mathrm{Li}}$ is the total electronic spin with projection m_{tot}.

We also note that there exist conical intersections between the ground and first excited doublet PESs at geometries that lie in the C_{2v} plane. Fortunately, these intersection points occur at energies that are classically forbidden for our Li+H_2 entrance channels. The collisional complex thus has negligible probability of occupying this configuration.

The use of the coupled basis in Eq. (7) is a natural consequence of the aforementioned approximations. In essence, the H_2 electronic spin S and m_S are zero in Eq. (6) and H_{hf} does not couple basis states, i.e., H_{hf} does not couple hyperfine states of lithium and H_2 and only leads to coordinate-independent shifts to the Hamiltonian. Thus, the orbital angular momentum $\vec{J} = \vec{j} + \vec{\ell}$ is a conserved quantity along with its projection M.

APPENDIX B: DEFINITIONS FOR SCATTERING RATE COEFFICIENTS

Our coupled-channel calculation provides S-matrix elements $s^{(J)}_{\alpha',\alpha}$, which we are used to construct rate coefficients. Here $\alpha = \{v, j, \ell\}$, $\alpha' = \{v', j', \ell'\}$, and J is the total angular momentum quantum number. In particular, we require the energy-dependent state-to-state rate coefficient

$$K_{v'j',vj}(E) = \frac{1}{2j+1} u_{vj} \frac{\pi}{k_{vj}^2} \sum_{J\ell\ell'} (2J+1) \left|\delta_{\alpha',\alpha} - s^{(J)}_{\alpha',\alpha}(E)\right|^2, \tag{B1}$$

where $u_{vj} = \sqrt{2(E - \epsilon_{vj})/\mu}$ is the relative velocity of the initial state and $k_{vj} = \mu\, u_{vj}/\hbar$ is the relative wave number. In the derivation of $K_{v'j',vj}(E)$, we have made use of the fact that the m_j sublevels in the rovibrational state $|v, jm_j\rangle$ of H_2 have equal population. The factor $1/(2j+1)$ is included in the definition of $K_{v'j',vj}(E)$ so that rate coefficients for different j can be compared directly as in Fig. 4. Elastic rate coefficients have $v'j' = vj$, while inelastic ones have $v'j' \neq vj$.

With this definition and assuming a Maxwell-Boltzmann distribution for both Li and H_2, the thermalized CAVS rate coefficient is

$$K^{\mathrm{CAVS}}(T_{\mathrm{Li}}, T_{\mathrm{H_2}}) = \sum_{vj} (2j+1)[2 - (-1)^j] \times \sum_{v'j'} L_{v'j',vj}(T_{\mathrm{Li}}, T_{\mathrm{H_2}}) \tag{B2}$$

with thermally averaged state-to-state rate coefficients

$$L_{v'j',vj}(T_{\mathrm{Li}}, T_{\mathrm{H_2}}) = \frac{1}{Z_{\mathrm{int}}} e^{-\epsilon_{vj}/k_{\mathrm{B}}T_{\mathrm{H_2}}} \frac{2}{\sqrt{\pi}} \int_0^\infty \sqrt{\zeta}\, d\zeta\, K_{v'j',vj} \times (\zeta k_{\mathrm{B}} T_{\mathrm{eff}} + \epsilon_{vj}) e^{-\zeta}, \tag{B3}$$

effective temperature

$$T_{\mathrm{eff}} = \frac{m_{\mathrm{H_2}}}{m_{\mathrm{Li}} + m_{\mathrm{H_2}}} T_{\mathrm{Li}} + \frac{m_{\mathrm{Li}}}{m_{\mathrm{Li}} + m_{\mathrm{H_2}}} T_{\mathrm{H_2}}, \tag{B4}$$

scaled relative kinetic energy ζ, and partition function

$$Z_{\mathrm{int}} = \sum_{\{vjmIm_I\}} e^{-\epsilon_{vj}/k_{\mathrm{B}}T_{\mathrm{H_2}}} \tag{B5}$$

$$= \sum_{vj} (2j+1)[2 - (-1)^j] e^{-\epsilon_{vj}/k_{\mathrm{B}}T_{\mathrm{H_2}}} \tag{B6}$$

for the internal degrees of freedom. The factor of $[2 - (-1)^j]$ is a consequence of the nuclear spin degeneracy for even and odd j. The curly brackets around the indices in Eq. (B5) indicate symmetrization and $T_{\mathrm{Li}} \ll T_{\mathrm{eff}} < T_{\mathrm{H_2}}$.

APPENDIX C: COMPARISON OF ELECTRONIC STRUCTURE METHODS

The PESs can be computed using several combinations of post-self-consistent-field methods and basis sets. For sufficiently large basis sets and increasing complexity of excitations, these methods should agree; however, as the basis set and number of correlated electrons gets larger the computational cost will become impractical. Our computational resources do allow us to compute the PESs for a small number of geometries R, r, and θ with the most accurate methods and basis sets available to us and compare them to more tractable computations. We can then verify the common practice to correct for the basis superposition error (BSSE) to account

[1] The $a\,^3\Sigma_u{}^+$ potential of H_2 does not support bound states [43].

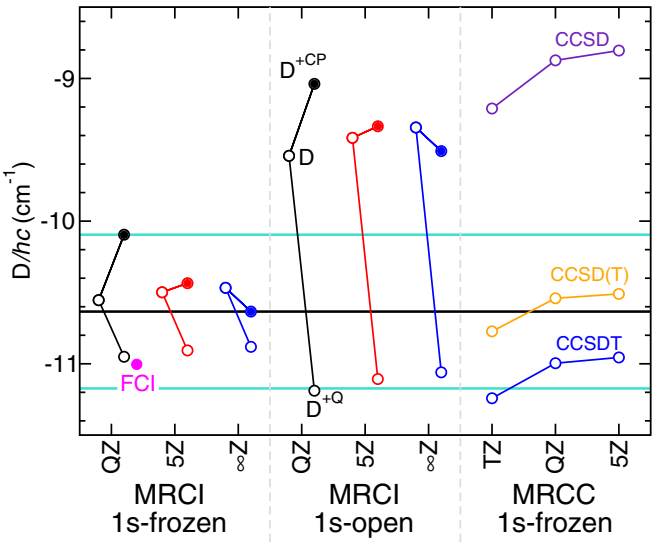

FIG. 7. Comparison of potential depths D for several combinations of post-self-consistent-field methods and basis sets with fixed $R = 10.0a_0$, $r = 1.4a_0$, and $\theta = 90°$. From left to right, the first set of three curves represents CASSCF and MRCI calculations with the 1s orbital of Li frozen and closed. The second set represents calculations with all electrons active and excitations from the 1s orbital are permitted. In both sets, the black and red curves are determined using the QZ and 5Z basis sets, respectively. The blue curve is the CBS extrapolation labeled by ∞Z. The leftmost marker on each curve is the uncorrected value D. The other two connected markers include the counterpoise (D^{+CP}, closed circle) and Davidson (D^{+Q}, open circle) corrections, respectively. The pink closed circle is the value from a full CI calculation with the QZ basis. The rightmost set of three curves shows D computed with the coupled-cluster method using the MRCC program of Kállay *et al.* [44] with the same basis as for the MRCI calculations and the 1s orbital of Li frozen (for clarity, predictions for the TZ basis within MRCI are not shown). The CCSD curve corresponds to a CC calculation with single and double excitations. The CCSD(T) curve adds perturbative triple excitations. Finally, the curve labeled CCSDT has all single, double, and triple excitations. The thick black horizontal line is our best prediction for D for $R = 10.0a_0$, $r = 1.4a_0$, and $\theta = 90°$. Horizontal turquoise lines indicate the 1-σ confidence interval.

for size-consistency and size-extensivity corrections and to extrapolate to the CBS for these geometries and set an appropriate uncertainty. In the following, we study how the depth of the potential at a T-shaped geometry, close to the minimum or optimized geometry, changes as we make different choices. Changes in this depth are a proxy for the accuracy of the PES. [This depth should not be confused with the related depth of the isotropic strength function $V_{\lambda=0}(R, r)$ defined in the main text.] For simplicity, we use TZ, QZ, and 5Z to abbreviate the basis-set labels aug-cc-pwCVTZ, aug-cc-pwCVQZ, and aug-cc-pwCV5Z for Li and aug-cc-pVTZ, aug-cc-pVQZ, and aug-cc-pV5Z for H, respectively.

Figure 7 shows the potential depth D for a T-shaped configuration, where $R = 10.0a_0$, $r = 1.4a_0$, and $\theta = 90°$. We compare three distinct approaches. The first two use MRCI to include electron correlations, while the third uses a coupled-cluster (CC) method. The distinction between the MRCI approaches is that the first freezes the inner 1s electrons of Li, while the other does not. In the CC calculations the 1s electrons of Li are also frozen. For each case, we compute D for the TZ, QZ, and 5Z bases.

The depth D from the all-electron MRCI calculations is found to be shallower than that from the corresponding frozen MRCI calculations when no corrections are applied. In contrast, the CC calculations show a progression to larger D as the number of excitations is increased from singles and doubles (CCSD) to triple excitations (CCSDT). As in the frozen calculations only three electrons are correlated, the CCSDT calculations is "exact." Indeed, as shown in Fig. 7, a full configuration-interaction (FCI) calculation for D using the QZ basis is consistent with CCSDT.

Full configuration-interaction and CCSDT calculations are computationally expensive and impractical for computing our PES for all grid points. The Davidson correction added to an MRCI calculation is a common procedure to approximate the full configuration interaction. This procedure attempts to account for size consistency and size extensivity. Indeed, our Davidson-corrected MRCI values D^{+Q} in Fig. 7 are much closer to the FCI and CCSDT predictions. The magnitude of the Davidson correction is about a factor of 3 larger in the all-electron case, which is a reflection of the size extensivity of MRCI. Nevertheless, the Davidson-correction brings the frozen and all-electron depths to within $hc \times 0.25\ \mathrm{cm}^{-1}$.

A second correction accounts for the BSSE. The BSSE arises as a result of limitations on the description of the atomic orbitals. We use the counterpoise correction algorithm of Ref. [33] to account for this error as mentioned in the main text. As the number of atomic orbitals (or size of the basis set) increases, the CP correction becomes smaller. Figure 7 shows that the CP correction to D from the 5Z basis set for the MRCI calculations is small compared to that for the QZ basis. The complete-basis-set extrapolation for D, Davidson-corrected D^{+Q}, and the CP-corrected D^{+CP} is computed from the TZ, QZ, and 5Z values using Eq. (11) and shown in Fig. 7 with label ∞Z.

The computation of the 8151 R, r, and θ geometries using the 5Z basis is the most demanding. As such, the only reasonable choice is performing MRCI calculations with frozen 1s electrons for Li. Other choices result in runtimes that are an order of magnitude or more larger. This leaves the determination of the uncertainty of the PES. We take the CBS-extrapolated D^{+CP} from MRCI calculations as our best prediction for the depth and take the one-standard-deviation uncertainty of the depth as the difference in D^{+CP} between the QZ and CBS extrapolated values, with the intent of placing a conservative error bar. These choices span all other predictions for the depth using QZ and 5Z basis sets, except for the uncorrected D and D^{+CP} for the all-electron MRCI and CCSD predictions. The exclusion of these latter predictions is justified as corrections due to higher-order correlations (triple and higher) are significant as shown by the larger depth for the all-electron MRCI D^{+Q} and CCSDT predictions. Additionally, Refs. [35,45] have shown that uncorrected all-electron basis calculations are less accurate than corresponding frozen-core calculations. In Sec. V we show how our uncertainty for a single geometry is translated into an uncertainty of the PES for all geometries and consequently for the rate coefficients.

APPENDIX D: NUMERICAL REPRESENTATION OF THE POTENTIAL ENERGY SURFACE AND MATRIX ELEMENTS

The choice of grid for R, r, and θ on which the PES is computed has been optimized for our scattering calculations to minimize the need for interpolation. In particular, the grid for θ is based on Gauss-Legendre quadrature, the grid for r is equally spaced between $r_{\min}$ and $r_{\max}$ around the equilibrium separation of the H_2 molecule, and the grid in R is separated in two regions, where in each region the grid is equidistant with a different spacing.

The nonequidistant Gauss-Legendre quadrature points for θ are found from $\cos\theta_i = x_i$, where the x_i are the roots of the Legendre polynomial with degree $\lambda_{\max}+1$, where $\lambda_{\max}$ is the highest degree used in the expansion in Eq. (12). We find it sufficient to set $\lambda_{\max} = 21$. The potential is invariant under hydrogen atom exchange, therefore the $V_\lambda(R,r)$ are only nonzero for even λ and we need only compute the PES for the eleven $\theta_i \in [0,\pi/2]$. The radial strength functions are then simply given by $V_\lambda(R,r) = \sum_i w_i\, U(R,r,\theta_i) P_\lambda(x_i)$, where w_i are the weights of the quadrature.

The grid in r is motivated by the procedure to calculate $\Xi^\lambda_{v'j',vj}(R)$ in Eq. (14). We use a discrete-variable representation (DVR) [46] to compute the eigenpairs ϵ_{vj} and $\phi_{vj}(r)$ of H_{H_2}. The grid for this DVR is equidistant and must have four or five points per oscillation in $\phi_{vj}(r)$. We include vibrational levels up to $v=2$, as its energy is approximately $k_B \times 15\,000$ K above the $v=0$ state and well above room-temperature collisional energies. We choose $r_{\min} = 0.5a_0$ and $r_{\max} = 2.5a_0$ with spacing $0.1a_0$ leading to 19 grid points. Figure 1(b) shows the relevant rovibrational eigenenergies and some of the radial wave functions of H_{H_2}. The integration in Eq. (14) over r is done using the quadrature for this DVR.

The $C_{6,0}(r)$ dispersion coefficient and ratio $\gamma(r) \equiv C_{6,2}(r)/C_{6,0}(r)$ have been computed by Thakkar *et al.* [39] from $r = 1.0a_0$ to $4.0a_0$ in steps of $0.2a_0$. The authors report a 0.1% one-standard-deviation uncertainty in $C_{6,0}(r)$. For $1.0a_0 < r < r_{\max}$, we interpolate using the Akima spline [47]. For grid points $r < 1.0a_0$, we linearly extrapolate $\gamma(r)$ and compute $C_{6,0}(r)$ from the dynamic polarizabilities of H_2 and Li at imaginary frequencies and integrating the Casimir-Polder-type integral [38]. The dynamic polarizability of H_2 is computed using CFOUR at the CCSD level, while that of Li is taken from Ref. [38]. Our computed $C_{6,0}(r)$ for $r < 1.0a_0$ is uniformly shifted to smoothly connect to that of Ref. [39] at $r = 1.0a_0$. This shift is less than 5% of its value. We verified that the shift does not affect our final rate coefficients within the quoted uncertainties.

Finally, our grid in R is constrained by the shape of the PES and the connection procedure to its long-range analytical form. We choose a grid starting at $R = 3.5a_0$ with increments of $0.5a_0$ up until $R = 15a_0$, where the increments increase to $1.0a_0$ up to $R = 30.0a_0$. The intent is to only use points up to $R_C < 30a_0$ and use the long-range form of $U(R,r,\theta)$ for $R > R_C$. The finer grid spacing at smaller R is required as the potential is changing more rapidly there.

We choose $R_C = 20.0a_0$. At this separation the short-range potential $V_{\lambda=0}(R_C,r) - V_{H_2}(r)$ is approximately $hc \times 0.05$ cm^{-1} deeper than the long-range $-C_{6,0}(r)/R_C^6$ form,

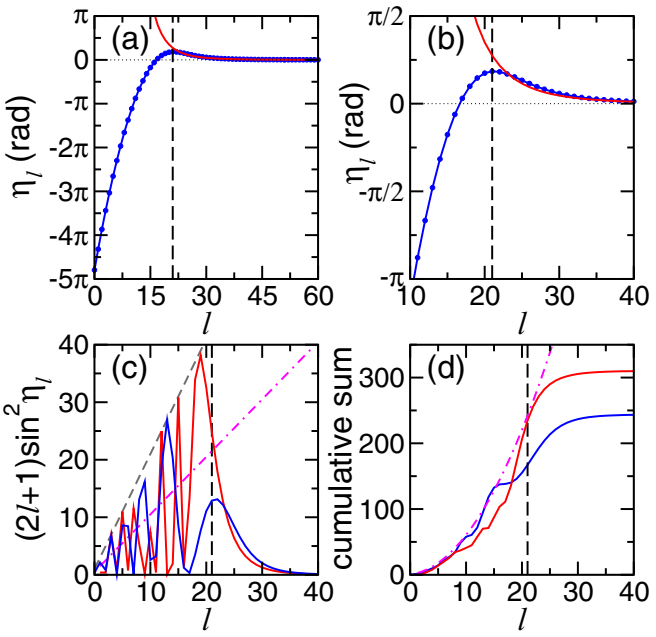

FIG. 8. (a) Elastic phase shift η_ℓ as a function of partial wave ℓ for the scattering of ^{6}Li with a $v = j = 0$ H_2 molecule at energy $E = \epsilon_{v=0,j=0} + k_B \times 300$ K. Here and in all panels, the blue curve corresponds to the coupled-channel phase shift $\eta_\ell^{CC}(E)$ extracted from the S matrix using only the $\lambda = 0$ strength function from the 5Z potential energy surface and the red curve is the Born-approximation prediction for the phase shift $\eta_\ell^{BA}(E)$ based on the long-range dispersion potential, defined in the text. The vertical dashed black line is the glory partial wave ℓ_g, where $\eta_\ell^{CC}(E)$ has a maximum. (b) Close-up of the phase shifts in (a) focusing on the region around ℓ_g. (c) Plot of $(2\ell+1)\sin^2\eta_\ell(E)$ as a function of ℓ. The dashed gray and magenta dot-dashed lines are the curves $2\ell+1$ and $(2\ell+1)/2$, respectively. (d) Cumulative sum over ℓ of (c). The magenta dot-dashed line corresponds to $\sum_{\ell'=0}^{\ell}(2\ell'+1)/2 = (\ell+1)^2/2$.

nearly independent of r. The difference in $V_{\lambda=0}(R_C,r)$ can be made smaller by adding higher-order multipolar contributions $-C_{n,\lambda}(r)/R^n$ for $n \geqslant 8$. In practice, however, we find it sufficient to connect matrix elements $\Xi^\lambda_{v'j',vj}(R)$ for all λ, v, j, v', and j'. Specifically, we add $-c^\lambda_{v'j',v,j}/R^8$ to the long-range form of $\Xi^\lambda_{v',j',v,j}(R)$, computed from the $-C_{6,\lambda}(r)/R^6$ potential, with the $c^\lambda_{v'j',v,j}$ as fitting parameters.

We have verified that this connection procedure does not affect our rate coefficients significantly, i.e., does not add to our quoted uncertainties. First, we find that the fitted values $c^\lambda_{v'j',v,j}$ are not unrealistic. We have computed $C_{8,\lambda}(r)$ coefficients at $r = r_e$ by using the multipolar polarizabilities of H_2 from Ref. [48] and Li from Ref. [38]. At $R = R_C$, this additional potential lowers the dispersion potential by $hc \times 0.1$ cm^{-1}, significantly reducing the discrepancy between the short- and long-range representations. The fitted $c^\lambda_{v'j',v,j}$ are only 30% larger than the corresponding matrix elements obtained from $-C_{8,\lambda}(r_e)/R^8$. For $\lambda > 0$, the differences between the short- and long-range forms are much smaller and also in line with the expected $-C_{8,\lambda}(r_e)/R$ contribution. (For $\lambda > 2$, the long-range potentials fall off as $1/R^8$ or faster.)

Second, we computed $K_{v'j',vj}(E)$ for a potential with $C_{6,\lambda}(r)$ values that are 5% larger than those of Thakkar *et al.* [39], well outside their quoted uncertainties. The $c^{\lambda}_{v'j',v,j}$ are again fitted. The resulting change in $K_{v'j',vj}(E)$ is less than 0.1% for all energies and rovibrational states and is an order of magnitude smaller than our final quoted uncertainty. This implies that neither the uncertainty in $C_{6,\lambda}(r)$ nor the fitting procedure significantly affects our rate coefficients.

APPENDIX E: DISAGREEMENT BETWEEN THE BORN APPROXIMATION AND COUPLED-CHANNEL RATE COEFFICIENTS

Figure 4 shows that there exists a significant discrepancy in $K_{vj,vj}(E)$ between the prediction from the Born approximation and the coupled-channel result. To understand this difference we analyze the partial wave scattering phase shifts $\eta_\ell(E)$ for the two cases. The coupled-channel phase shift $\eta_\ell^{\rm CC}(E)$ can be extracted from the diagonal matrix element $s^{(J)}_{\alpha,\alpha}(E)$, when only the $\lambda = 0$ strength function is included in the calculations. The S matrix is then diagonal in our basis $|v(j,\ell)JM\rangle$ and $s^{(J)}_{\alpha,\alpha}(E) = \exp[2i\eta_\ell^{\rm CC}(E)]$. The value of $K_{vj,vj}(E)$ based on this approximation agrees to within 1% of the full calculation as discussed in Sec. IV. For an isotropic potential, the Born approximation of the phase shift is [41]

$$\eta_\ell^{\rm BA}(E) = \frac{3\pi}{32}\left(\frac{E}{E_6}\right)^2 \frac{1}{\ell^5} \tag{E1}$$

and only depends on the potential's attractive $-C_{6,0}/R^6$ long-range shape.

Figures 8(a) and 8(b) show both $\eta_\ell^{\rm BA}(E)$ and $\eta_\ell^{\rm CC}(E)$ as functions of partial wave ℓ at a single collision energy $E = k_{\rm B} \times 300$ K. The two phase shifts agree for $\ell > 30$. This is not surprising as large-ℓ scattering is dominated by the centrifugal and long-range potentials as the short-range parts of the potential are classically forbidden. For smaller values of ℓ, both phase shifts rapidly change over multiple π phases. The stationary point of $\eta_\ell^{\rm CC}(E)$ at $\ell = \ell_g = 21$ is called the glory partial wave [41]. The change in phase shift from $\ell = \ell_g$ to $\ell = \infty$ is less than $\pi/2$. In contrast, in many bi-alkali-metal collisions this difference is many π.

Figures 8(c) and 8(d) show $(2\ell+1)\sin^2\eta_\ell(E)$ and its cumulative sum as functions of ℓ, respectively. The former corresponds to the ℓ-dependent contributions to $K_{vj,vj}(E)$ [up to the simple factor $u_{v,j}\pi/k^2_{vj}/(2j+1)$] and for $\ell < \ell_g$ rapidly oscillates between 0 and $2\ell+1$, the unitarity limit for partial wave ℓ. For larger ℓ the contribution rapidly falls off. The cumulative sum approaches $K_{vj,vj}(E)$ (up to the same simple factor) for $\ell \to \infty$. The contributions to $K_{vj,vj}(E)$ from partial waves $\ell < 15$ and $\ell > 25$ for the Born approximation and the coupled-channel results are approximately equal. For $\ell < 15$ the phase shifts change over multiple π as a function of ℓ and we can replace $\sin^2\eta_\ell$ by $1/2$, its average, for any potential, as shown in the figure. For $\ell > 25$ the Born-approximation and the coupled-channel contributions are the same by construction. The main difference is due the partial waves around ℓ_g, which here corresponds to roughly a third of the rate. In contrast, in bi-alkali-metal collisions the contribution from these partial waves is small and the Born approximation is valid.

[1] S. R. Jefferts, J. Shirley, T. E. Parker, T. P. Heavner, D. M. Meekhof, C. Nelson, F. Levi, G. Costanzo, A. D. Marchi, R. Drullinger *et al.*, Metrologia **39**, 321 (2002).

[2] J. Scherschligt, J. A. Fedchak, D. S. Barker, S. Eckel, N. Klimov, C. Makrides, and E. Tiesinga, Metrologia **54**, S125 (2017).

[3] S. Eckel, D. S. Barker, J. A. Fedchak, N. N. Klimov, E. Norrgard, J. Scherschligt, C. Makrides, and E. Tiesinga, Metrologia **55**, S182 (2018).

[4] R. T. Bayard and D. Alpert, Rev. Sci. Instrum. **21**, 571 (1950).

[5] F. Dalfovo, S. Giorgini, L. P. Pitaevskii, and S. Stringari, Rev. Mod. Phys. **71**, 463 (1999).

[6] J. H. Denschlag, J. E. Simsarian, H. Häffner, C. McKenzie, A. Browaeys, D. Cho, K. Helmerson, S. L. Rolston, and W. D. Phillips, J. Phys. B **35**, 3095 (2002).

[7] I. Bloch, J. Dalibard, and W. Zwerger, Rev. Mod. Phys. **80**, 885 (2008).

[8] A. L. Migdall, J. V. Prodan, W. D. Phillips, T. H. Bergeman, and H. J. Metcalf, Phys. Rev. Lett. **54**, 2596 (1985).

[9] O. J. Luiten, M. W. Reynolds, and J. T. M. Walraven, Phys. Rev. A **53**, 381 (1996).

[10] D. E. Fagnan, J. Wang, C. Zhu, P. Djuricanin, B. G. Klappauf, J. L. Booth, and K. W. Madison, Phys. Rev. A **80**, 022712 (2009).

[11] M. Strebel, T.-O. Müller, B. Ruff, F. Stienkemeier, and M. Mudrich, Phys. Rev. A **86**, 062711 (2012).

[12] J. E. Bjorkholm, Phys. Rev. A **38**, 1599 (1988).

[13] E. A. Burt, R. W. Ghrist, C. J. Myatt, M. J. Holland, E. A. Cornell, and C. E. Wieman, Phys. Rev. Lett. **79**, 337 (1997).

[14] S. Bali, K. M. O'Hara, M. E. Gehm, S. R. Granade, and J. E. Thomas, Phys. Rev. A **60**, R29 (1999).

[15] T. Arpornthip, C. A. Sackett, and K. J. Hughes, Phys. Rev. A **85**, 033420 (2012).

[16] V. B. Makhalov, K. A. Martiyanov, and A. V. Turlapov, Metrologia **53**, 1287 (2016).

[17] J.-f. Xiang, H.-n. Cheng, X.-k. Peng, X.-w. Wang, W. Ren, J.-w. Ji, K.-k. Liu, J.-b. Zhao, L. Li, Q.-z. Qu *et al.*, Chin. Phys. B **27**, 073701 (2018).

[18] K. Gibble, Phys. Rev. Lett. **110**, 180802 (2013).

[19] G. Pagano, P. W. Hess, H. B. Kaplan, W. L. Tan, P. Richerme, P. Becker, A. Kyprianidis, J. Zhang, E. Birckelbaw, M. R. Hernandez *et al.*, Quantum Sci. Technol. **4**, 014004 (2019).

[20] S. Bovino, M. Tacconi, F. A. Gianturco, D. Galli, and F. Palla, Astrophys. J. **731**, 107 (2011).

[21] P. C. Stancil, S. Lepp, and A. Dalgarno, Astrophys. J. **458**, 401 (1996).

[22] M. Wernli, D. Caruso, E. Bodo, and F. A. Gianturco, J. Phys. Chem. A **113**, 1121 (2009).

[23] J. Yuan, D. He, and M. Chen, Phys. Chem. Chem. Phys. **17**, 11732 (2015).

[24] J. M. Hutson, in *Advances in Molecular Vibrations and Collision Dynamics*, edited by J. M. Bowman and M. A. Ratner (JAI, Greenwich, 1991), p. 1.
[25] J. Loreau, P. Zhang, and A. Dalgarno, J. Chem. Phys. **135**, 174301 (2011).
[26] D. M. Brink and G. R. Satchler, *Angular Momentum* (Clarendon, Oxford, 1994).
[27] B. Johnson, J. Comput. Phys. **13**, 445 (1973).
[28] J. R. Taylor, *Scattering Theory: The Quantum Theory of Nonrelativistic Collisions* (Dover, New York, 2012).
[29] H.-J. Werner, P. J. Knowles, G. Knizia, F. R. Manby, M. Schütz, P. Celani, W. Györffy, D. Kats, T. Korona, R. Lindh *et al.*, MOLPRO, version 2018.1, a package of *ab initio* programs 2018, http://www.molpro.net.
[30] T. H. Dunning, J. Chem. Phys. **90**, 1007 (1989).
[31] R. A. Kendall, T. H. Dunning, and R. J. Harrison, J. Chem. Phys. **96**, 6796 (1992).
[32] B. P. Prascher, D. E. Woon, K. A. Peterson, T. H. Dunning, and A. K. Wilson, Theor. Chem. Acc. **128**, 69 (2011).
[33] S. Boys and F. Bernardi, Mol. Phys. **19**, 553 (1970).
[34] K. A. Peterson, D. E. Woon, and T. H. Dunning, J. Chem. Phys. **100**, 7410 (1994).
[35] M. P. de Lara-Castells, R. V. Krems, A. A. Buchachenko, G. Delgado-Barrio, and P. Villarreal, J. Chem. Phys. **115**, 10438 (2001).
[36] I. C. Percival and M. J. Seaton, Math. Proc. Cambridge **53**, 654 (1957).
[37] C. Zhu, A. Dalgarno, and A. Derevianko, Phys. Rev. A **65**, 034708 (2002).
[38] A. Derevianko, S. G. Porsev, and J. F. Babb, At. Data Nucl. Data Tables **96**, 323 (2010).
[39] A. J. Thakkar, Z.-M. Hu, C. E. Chuaqui, J. S. Carley, and R. J. LeRoy, Theor. Chim. Acta **82**, 57 (1992).
[40] See Supplemental Material at http://link.aps.org/supplemental/10.1103/PhysRevA.99.042704 for data files.
[41] M. S. Child, *Molecular Collision Theory* (Dover, New York, 1974).
[42] N. F. Mott and H. S. W. Massey, *Theory of Atomic Collisions* (Oxford University Press, Oxford, 1985).
[43] W. Kołos and L. Wolniewicz, J. Chem. Phys. **43**, 2429 (1965).
[44] M. Kállay, Z. Rolik, J. Csontos, P. Nagy, G. Samu, D. Mester, J. Csóka, B. Szabó, I. Ladjánszki, L. Szegedy *et al.*, MRCC, a quantum chemical program suite, 2013.
[45] A. K. Wilson, D. E. Woon, K. A. Peterson, and T. H. Dunning, J. Chem. Phys. **110**, 7667 (1999).
[46] D. T. Colbert and W. H. Miller, J. Chem. Phys. **96**, 1982 (1992).
[47] H. Akima, J. ACM **17**, 589 (1970).
[48] D. M. Bishop and J. Pipin, Int. J. Quantum Chem. **47**, 129 (1993).